

Shear-driven motion of Mg $\{10\bar{1}2\}$ twin boundaries via disconnection terrace nucleation, growth, and coalescence

Douglas E. Spearot,^{1,*} Laurent Capolungo,² and Carlos N. Tomé²

¹*Department of Mechanical & Aerospace Engineering, University of Florida, Gainesville, Florida 32608, USA*

²*Materials Science and Technology Division, Los Alamos National Laboratory, Los Alamos, New Mexico 87545, USA*



(Received 7 March 2019; published 17 May 2019)

Twin nucleation and growth are prevalent plastic deformation mechanisms in hexagonal close-packed metals such as Mg. For twin growth to occur, the interfaces that border the twinned domain must migrate and the kinetics associated with this process are yet to be fully explained. Thus, the objective of this study is to characterize the relationship between the kinetics of the $\{10\bar{1}2\}$ twin boundary in pure Mg in the stress-driven regime, and the nucleation, growth, and coalescence of disconnection terraces that serve as the mechanisms for migration. This problem is addressed via atomistic simulations adopting both two- (2D) and three-dimensional (3D) simulation geometries, and a model for the velocity of the $\{10\bar{1}2\}$ twin boundary as a function of temperature and shear stress is proposed. This study shows that the kinetics of $\{10\bar{1}2\}$ twin boundary migration must be addressed using 3D models, as 2D simulations do not properly capture disconnection terrace nucleation and growth processes, demonstrated via differences in activation volumes and energies. Importantly, simulations reveal an autocatalytic terrace nucleation mechanism as playing a role in twin growth, where nucleation of a new terrace is dependent on the growth of existing terraces on the twin plane.

DOI: [10.1103/PhysRevMaterials.3.053606](https://doi.org/10.1103/PhysRevMaterials.3.053606)

I. INTRODUCTION

Deformation twinning plays a fundamental role in the mechanical behavior of hexagonal close-packed (hcp) metals [1]. In the process of accommodating plastic deformation, the morphology of the twin domains and their associated interfaces affects hardening, texture evolution, and ductility [2]. As a consequence, much work has been devoted in the past decade to study hcp twinning at all length scales experimentally, computationally, and theoretically. In particular, understanding the atomistic configuration and mobility of twin interfaces is an indispensable first step for elucidating the role of twinning in hcp plasticity. However, despite the fact that twins are three-dimensional (3D) domains [2,3], the majority of previous studies devoted to twin interface characterization regard twins as two-dimensional (2D) entities. One can draw a similitude between twin growth and Earth topography: Plate tectonics shows that mountain ridges form at subduction zones and 2D cross sections of the mantle depict clean elevation profiles in the continents. The 3D geological topography, however, is much less uniform and characterized by a rather inhomogeneous distribution of elevations and depressions.

The thickening of a $\{10\bar{1}2\}$ twin domain requires the motion of the $\{10\bar{1}2\}$ coherent interface [4,5]. Such motion is mediated by a shear stress, and it is well known that the interface does not displace as a whole in this process, but through the successive nucleation and motion of interfacial defects that propagate “steps” [6,7]. While all of these interfacial defects induce the same crystallographic shear, they can

have varying heights ranging from, at minimum, two interplanar spacings up to several dozen [7]. Depending on their character, these defects have been reported to be twinning dislocations, disconnections, or disclinations [7–10]. Away from triple lines and in the absence of grain boundary sliding, the shear coupling relationship $v_n\beta v_{||}$ is sometimes used [11] to describe the velocity of the interface in the direction of its normal vector, v_n , relative to the shearing velocity, $v_{||}$. The coupling factor β may be positive or negative and has been related to the crystallography of the mating lattices [11].

In 2D models, the steps are implicitly regarded as being of infinite length in one dimension by using periodic boundary conditions in atomistic simulations, even if the thickness of the simulation model is sufficient to allow for the nucleation of kink pairs [12]. In 3D, the steps become “terraces,” and the key scientific questions are as follows: How do they nucleate and how do they grow laterally within the twin boundary? The answers are relevant to the kinetics of propagation of twin boundaries, and this work will show that temperature and shear-stress dependence is measurably different for 3D than for 2D propagation.

Only a few prior groups have explored the nucleation of disconnection terraces in true 3D simulation models [13–15]. For example, Race *et al.* and Hadian *et al.* studied the nucleation of 3D terraces on a flat $\Sigma 7(111)$ symmetric tilt grain boundary (GB) in Al [13], and on asymmetric Al GBs which naturally contain steps or kinks as part of their interface structure [14]. First, they showed that large cells are necessary to attain convergence in the interface velocity. Then, using classical homogeneous nucleation theory, they showed that the energy barrier for the nucleation of a disconnection terrace on the $\Sigma 7(111)$ symmetric tilt GB was inversely proportional to the driving force imparted on the GB, leading to

*dspearot@ufl.edu

non-Arrhenius migration behavior. Their model, based on terrace nucleation [13], predicted an extremely large energy barrier and large critical terrace radius at low driving force, implying that atomically flat GBs have no intrinsic mobility. However, Hadian *et al.* later showed [14] that motion of asymmetric GBs occurs via motion of preexisting kinks within the GB, rather than terrace nucleation, and thus displayed an energy barrier for migration independent of driving force. Considering $\{10\bar{1}2\}$ twins in Mg and Mg alloys, Luque *et al.* [15] presented a model for twin boundary migration based on the concept of homogeneous terrace nucleation. Specifically, for the arbitrary assumption of a square terrace, they proposed an Arrhenius model for twin growth rate validated by molecular dynamics (MD) simulations at applied shear stresses between 15 and 100 MPa. MD simulations with these boundary conditions confirmed the mechanism of terrace nucleation and the assumption that twin boundary migration occurred by individual terrace nucleation events well separated in time. Note, while the above models are based on homogeneous nucleation, dislocation interactions with 2D and 3D twin interfaces can also lead to the heterogeneous nucleation of terraces, as reported for the 2D case by Serra and Bacon [16,17], and for the 3D case by Gong *et al.* [2].

Building upon prior efforts, the objective of this work is to characterize the mechanisms associated with migration of the coherent $\{10\bar{1}2\}$ mirror twin boundary in Mg in the shear-stress-driven regime between 100 and 500 MPa, using 2D and 3D atomistic simulation models. In this sense, this work explores twin boundary migration mechanisms in a fundamentally different regime as that explored by Luque *et al.* [15]. Resolved shear stresses greater than 100 MPa are certainly plausible on the local scale. For example, the shear transformation associated with the tensile twin, in excess of 12%, will induce stresses near the twin interface and at the twin tip reaching far more than 100 MPa [18]. Similarly, these high local stresses will occur during high rate loading and due to interactions between the twin domain and other defects [18–20]. This work finds that twin propagation is mediated by the nucleation, growth, and coalescence of terraces, which are delimited by elementary $b_{2/2}$ disconnections [17], consistent with prior work [13–15]. Furthermore, the details of terrace nucleation are affected by the 2D versus 3D nature of the atomistic simulation models. A model for the velocity of the $\{10\bar{1}2\}$ twin boundary across the range of temperatures and shear stresses evaluated is presented. Using this model, average activation energies and activation volumes are computed for disconnection-based mechanisms in both 2D and 3D growth simulations. This study unambiguously shows that 3D simulations are necessary to quantify the kinetics of twin propagation, in agreement with length scale convergence simulations reported by Race *et al.* for a flat $\Sigma 7(111)$ symmetric tilt grain boundary in Al [13]. A novel result in this work is the observation of an autocatalytic terrace nucleation mechanism occurring within the range of shear stresses and temperatures explored, whereby stress concentrations associated with the presence and growth of existing terraces on the twin boundary promote the nucleation of new terraces. Such a process can be revealed only at shear stresses or temperatures that allow for correlated (rather than uncorrelated [15]) migration mechanisms on the twin boundary. The effective activation

volume and energy associated with the nucleation of terraces are computed to be very small, $<0.26b^3$ and <0.1 eV, respectively, and different values for these parameters are found for 2D and 3D simulation models. Note that the term autocatalytic has been used recently [21] to describe nucleation of a new twin from a grain boundary source, due to the local stress field of an incoming twin [22]. This work shows that the twin thickening process itself can be autocatalytic in nature. Altogether, this study delineates the importance of accounting for local stress concentrations (which may include intergranular and intragranular interactions) in the vicinity of twin boundaries, in order to quantify the kinetics of twinning.

II. METHODS

A. Simulation codes and interatomic potential

Atomistic simulations in this work are performed using LAMMPS [23] with atomic visualizations generated using OVITO [24]. The modified embedded-atom method (MEAM) potential for Mg developed by Wu *et al.* [25] is used for all simulations. This MEAM potential provides a more accurate description of Mg lattice parameters, cohesive energy, and defect energies, compared to an earlier MEAM potential by Kim *et al.* [26]. Further, since the MEAM potential accounts for angular dependence of atomic bonding, it is more appropriate for hcp Mg than earlier embedded-atom method (EAM) potentials by Sun *et al.* [27] or Zhou *et al.* [28]. For example, the EAM potential by Sun *et al.* provides an unrealistic stacking fault energy and predicts that the $\{10\bar{1}2\}\langle 1011 \rangle$ twinning dislocation is unstable [25].

B. 2D and 3D simulation models

Figure 1 shows the simulation geometry employed in this work. The lattice regions are oriented such that the $\{10\bar{1}2\}$ twin boundary lies parallel to the global XY plane. Periodic boundary conditions are employed in all directions, resulting in a second $\{10\bar{1}2\}$ twin boundary in the Z direction. For 2D models, $L_X = 0.3187$ nm, $L_Y = 30.35$ nm, and $L_Z = 49.35$ nm, while for 3D models, $L_X = 31.87$ nm with the Y and Z dimensions the same as the 2D model. The 3D model dimensions are larger than those used by Race *et al.* [13,14]; they proved that volumes of this size are sufficient to capture a converged response for terrace nucleation. Regardless, in the case of the 3D model, supplementary simulations with larger X and Y dimensions are performed to confirm that the disconnection-based mechanisms associated with shear-driven motion of the twin boundary are not adversely influenced by the size of the periodic simulation domain.

To determine the minimum energy structure of the $\{10\bar{1}2\}$ twin boundary, a standard procedure [29–31] is employed whereby the opposing lattice regions are translated relative to each other to provide different starting configurations for an energy minimization procedure. The extent of the translations in the Y and Z directions is motivated by the Gibbs potential energy surface determined via density functional theory (DFT) calculations [32]. At each starting configuration, sequential energy minimization calculations are performed using a nonlinear conjugate gradient method, with the simulation cell allowed to change size and shape to provide a

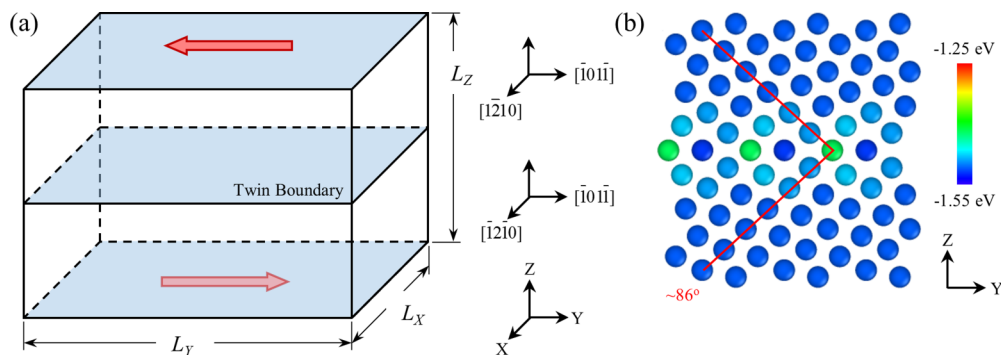


FIG. 1. (a) Schematic of the $\{10\bar{1}2\}$ twin boundary simulation cell. The global Z direction is normal to the twin boundary plane. (b) $\{10\bar{1}2\}$ Mirror twin boundary structure predicted using the MEAM potential of Wu *et al.* [25]. Atoms are colored by atomic potential energy.

stress-free atomistic model. Figure 1(b) shows the minimum energy structure of the $\{10\bar{1}2\}$ twin boundary. The twin boundary is atomically flat with an approximately 86° misorientation between basal planes in opposing grains, in agreement with prior DFT and atomistic simulation results [32–36].

C. Thermodynamic equilibration and shear deformation

After the equilibrium structure of the twin boundary is attained, a state of pure shear stress is applied ($\tau_{yz} \neq 0$ with all other stress components equal to zero) by allowing simulation cell size and shape changes during an energy minimization process. Then, the twin boundary model is brought to a desired temperature T , while maintaining the shear stress τ_{yz} , using MD simulations in the isostress-isothermal ($N\sigma T$) ensemble [37]. Temperatures between 100 and 400 K and shear stresses between 100 and 500 MPa are considered in this work. During equilibration, the twin boundary may begin to move. The MD simulations under a constant shear stress are continued for a sufficient amount of time to capture meaningful motion of the $\{10\bar{1}2\}$ twin boundary in the Z direction. The velocity of the twin boundary is computed from the average shear strain rate of the simulation cell, as explained in Sec. III. Each 2D simulation is repeated five times and each 3D simulation is repeated three times with different random thermal seeds for the initialization of the atomic velocities. Data presented are averages over the simulation sets. Note, with this approach, a state of pure shear stress is uniformly applied over the entire simulation cell without manually imposing shear displacements on the boundaries on the system in the Z direction. This differs from many prior atomistic simulations of shear-driven motion of grain boundaries where interface motion is induced via a shear displacement [8, 11, 12]. These approaches do not allow uniform control of the stress state acting on the interface, although the interface is guaranteed to move at any temperature if the shear displacement is continually increased.

III. RESULTS

A. Twin boundary motion in 2D models

Figure 2 shows shear strain and twin boundary velocity data for 2D simulations of shear-driven motion of the $\{10\bar{1}2\}$ twin boundary. Figure 2(a) shows shear strain as a function

of time step. The important aspect of this figure is the time domain over which the slope of shear strain versus time step curve is approximately linear, as this portion of the shear deformation process is used to compute average twin boundary velocity. The plateau in the shear strain observed around $\gamma_{yz} = -0.07$ for models with $T > 100$ K are solely a consequence of the height L_z of the simulation cell. Since the twin boundaries migrate in opposite directions, they will annihilate after each moves a distance of $L_z/4$. The result of the annihilation is a twin-boundary-free sample, and since the shear stress applied is below the critical shear stress for homogeneous defect nucleation, no additional shear strain is realized postannihilation.

To compute the average twin boundary velocity for each combination of temperature and shear stress, the shear strain rate $\dot{\gamma}$ is first computed using the displacement of the simulation cell along the shear direction, divided by time and the height of the cell, using a MD simulation time step of 0.001 ps. Then, the average twin boundary velocity is computed as $v = \dot{\gamma} L_z / 2\gamma_{tw}$, where L_z is the height of the simulation model containing two mirror twin boundaries and $\gamma_{tw} = 0.13$ is the plastic shear strain generated by a disconnection pair as it advances the boundary [15]. Since disconnection terrace nucleation and growth on the twin boundary planes is expected to be the only mechanism in operation, the average velocity of the twin boundary can be computed via this approach and direct tracking of the twin boundary Z elevations is not necessary.

Figure 2(b) shows the $\{10\bar{1}2\}$ twin boundary velocity as a function of inverse temperature for 2D simulations. Each data point represents the average of five independent 2D simulations with standard deviation of less than 8.6% for all data points. At the highest shear stresses imposed (highest driving forces), the data are linear and the slope (temperature dependence) indicates an Arrhenius-type behavior. This is in qualitative agreement with prior studies on the shear-coupled motion of grain boundaries in fcc materials [11, 13, 14]. However, at lower driving forces and lower temperatures, a decay in the shear strain rate is apparent, indicating a transition from a drag-controlled regime to a nucleation-controlled regime. Statistical variation between the five model realizations is much smaller than the magnitude of the low-temperature decay in the shear strain rate. This regime transition is evident in Fig. 2(a); at low temperature (100 K) and moderate shear stress (100 MPa), the shear strain evolves discontinuously

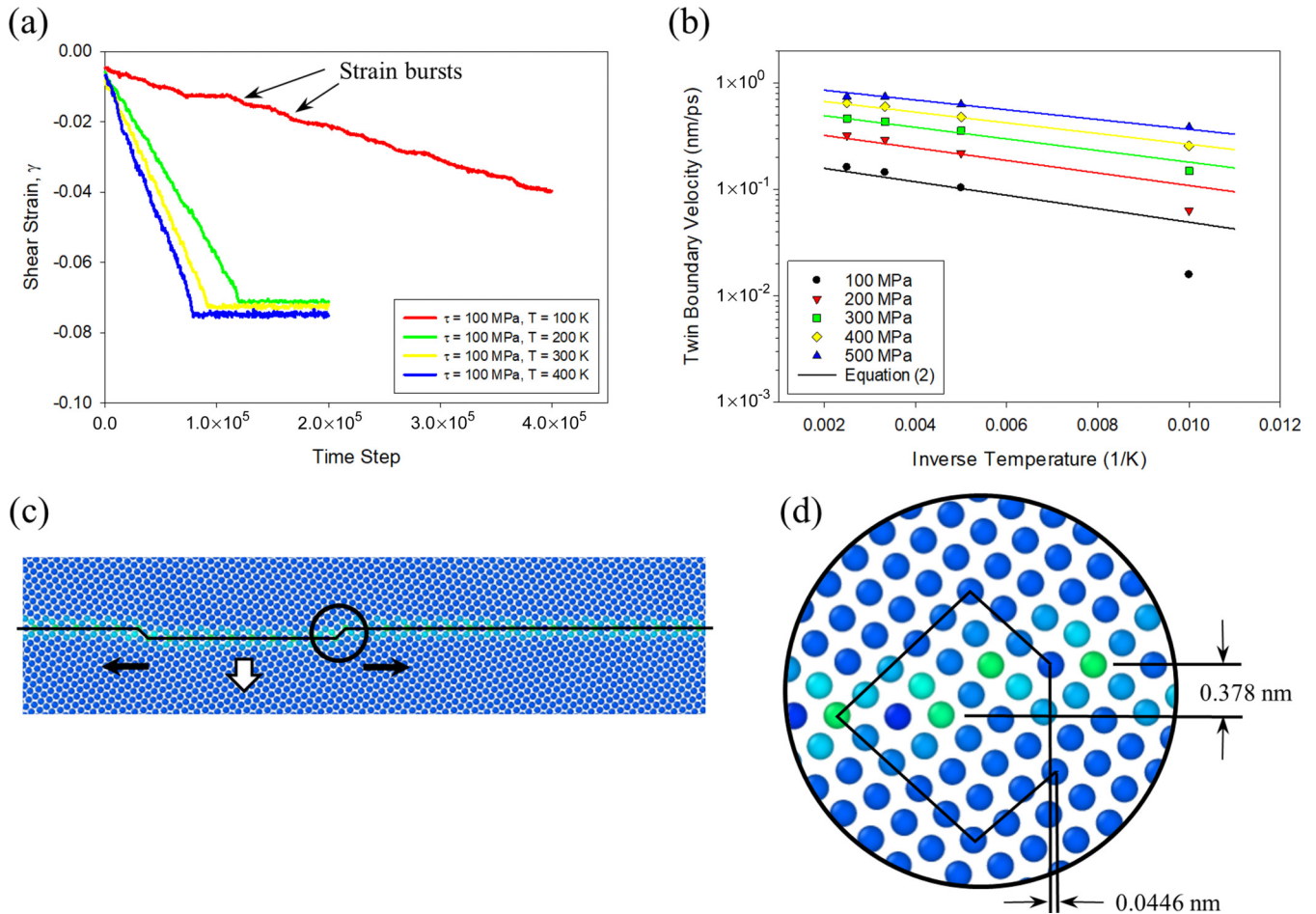


FIG. 2. (a) Shear strain as a function of time step for select 2D atomistic simulations. Individual nucleation events are visible at the lowest driving forces. (b) Average twin boundary velocity as a function of inverse temperature for 2D simulation models. The lines correspond to the model presented as Eq. (2) in Sec. III C. (c) Nucleation of disconnections on the twin boundary plane. Disconnections move in opposite directions (solid arrows) and coalesce at the periodic boundary to move the twin boundary down (open arrow) a distance equal to the disconnection step height. (d) Detail showing the crystallography of the disconnection step. Atoms are colored by atomic potential energy with the same scale as Fig. 1.

and strain bursts can be correlated with nucleation events [15]. Overall, the rate sensitivity of the $\{10\bar{1}2\}$ twin boundary motion process in 2D is not negligible. This fact is typically discarded in the literature, which usually assumes twinning to be an athermal and strain-rate-insensitive process.

The mechanisms by which the $\{10\bar{1}2\}$ twin boundaries migrate are shown in Figs. 2(c) and 2(d) for $\tau_{YZ} = 100$ MPa at $T = 100$ K. These images are created following a brief steepest descent energy minimization to eliminate thermal oscillations that obscure the view of the twin boundary. Shear-driven motion of the $\{10\bar{1}2\}$ twin boundary is initiated by the spontaneous nucleation of a pair of disconnections, as shown in Fig. 2(c). The disconnections propagate in opposite directions along the twin boundary plane and coalesce at the periodic boundary, moving the $\{10\bar{1}2\}$ twin boundary a distance equal to the step height of the disconnections. This process repeats to continue the motion of the twin boundary. The disconnections have a vertical step height 0.378 nm and a $\langle\bar{1}011\rangle$ dislocation with a Burgers vector of 0.0446 nm (based on analysis of the crystallography [38]), as shown in Fig. 2(d). The nucleation process is directional as disconnections are

nucleated on the negative Z face of the twin boundary in the center of the simulation cell, as shown in Fig. 2(c), while they are nucleated on the positive Z face of the twin boundary at the periodic border (not shown in Fig. 2). Reversing the sign of the applied shear stress, thereby reversing the sign of $v_{||}$, reverses the direction of twin migration. This basic mechanism is consistent for all temperatures and shear stresses considered, and is in qualitative agreement with prior works on shear-coupled grain boundary motion [8,12]. At high temperatures or driving forces, multiple disconnection pairs can nucleate simultaneously promoting reasonably smooth boundary motion. A similar result has been reported by Martinez *et al.* for 2D simulations of $\{10\bar{1}2\}$ twins in Ti [10]. This accelerated terrace nucleation rate is further discussed in a later section, within the framework of a model for shear stress and temperature dependent behavior.

B. Twin boundary migration in 3D models

It is expected that a generalization of the mechanism observed in 2D simulations would take place in 3D simulations.

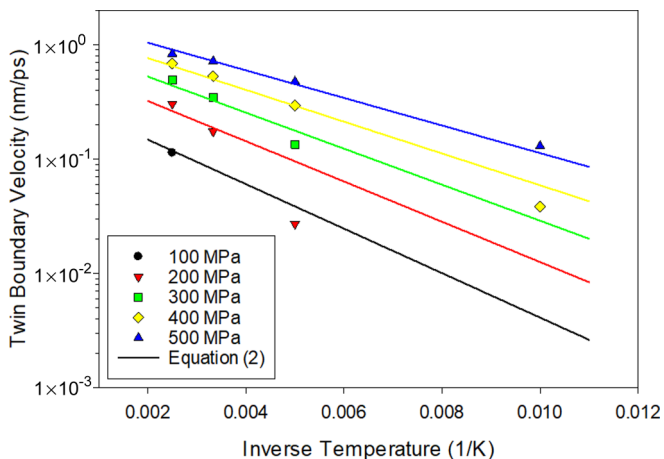


FIG. 3. Twin boundary velocity versus inverse temperature for 3D models. The lines correspond to the model presented as Eq. (2) in Sec. III C.

While this is the case, this section shows that the kinematics and kinetics are different, similar to the conclusions made by Race *et al.* for terrace nucleation on a symmetric tilt GB [13]. Figure 3 shows twin boundary velocity as a function of inverse temperature for 3D simulations of shear-driven motion of the {10 $\bar{1}2$ } twin boundary. Twin boundary velocity is computed using the same method as in the 2D simulations in Sec. III A. Each data point represents the average of three independent 3D simulations with standard deviation of less than 1.3% for most data points. The exceptions are models subjected to boundary conditions close to the nucleation-dominated regime where error based on standard deviation is at most 20.3%. For a few temperature and shear-stress combinations, the nucleation rate of disconnection terraces is particularly rate limiting such that twin boundary migration is out of reach

for the MD simulation times; these data are omitted from Fig. 3.

At high temperatures and driving forces, twin boundary motion exhibits Arrhenius behavior. However, at low temperatures, such as 100 K, a clear decline is apparent in the velocity. Visually, the slopes of the relationship between twin boundary velocity and inverse temperature are steeper in Fig. 3 for shear-driven motion of the {10 $\bar{1}2$ } twin boundary in 3D models than those shown in Fig. 2(b) for 2D models. This implies that an accurate description of nucleation and motion of disconnection terraces is not captured by 2D model geometries.

Figure 4 shows a view normal to the {10 $\bar{1}2$ } twin boundary, illustrating the mechanisms by which the twin boundary moves, for the case $\tau_{YZ} = 500$ MPa and $T = 100$ K. Shear-driven motion of the {10 $\bar{1}2$ } twin boundary is initiated by the nucleation of a small disconnection terrace, as shown in Fig. 4(a). In the direction normal to the twin boundary, the disconnection loop has a step height 0.378 nm and a $\langle\bar{1}011\rangle$ dislocation with Burgers vector magnitude 0.0446 nm, identical to that of the 2D model. In the $\langle\bar{1}2\bar{1}0\rangle$ direction, the disconnection loop contains only a pure step of 0.378 nm because this direction is common in the two crystals and thus no mismatch is required. Once the disconnection terrace is nucleated, it expands and coalesces with other terraces within the twin boundary plane, leading to movement of the twin boundary a distance equal to the step height. It is found that the first few terraces take on an approximately elliptical shape as they expand, implying that there is a dependence of mobility on the character angle of the disconnection, analogous to that found in dislocations [39,40]. Interestingly, very small terraces are found to nucleate ahead of moving terraces, identified at multiple snapshots in Fig. 4 with circles. This suggests that the nucleation of disconnection terraces can be conditional on prior history, i.e., the growth of existing

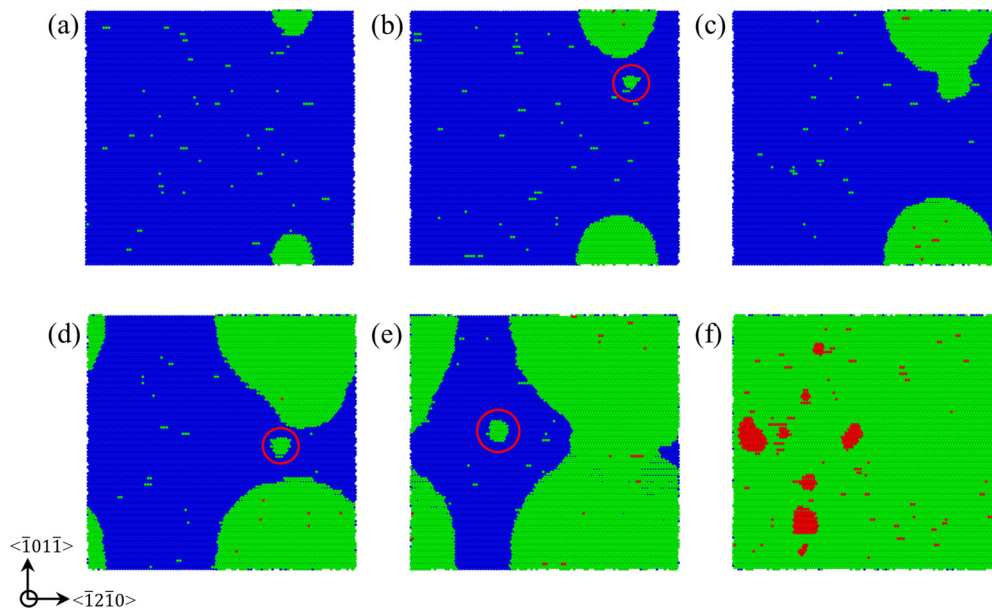


FIG. 4. Disconnection terrace nucleation, growth, and coalescence at 100 K with an applied shear stress of 500 MPa. Atoms are colored in bands by Z position with blue, green, and red colors representing different sets of {10 $\bar{1}2$ } planes parallel to the twin boundary. Regions of autocatalytic nucleation in the initial twin boundary are circled.

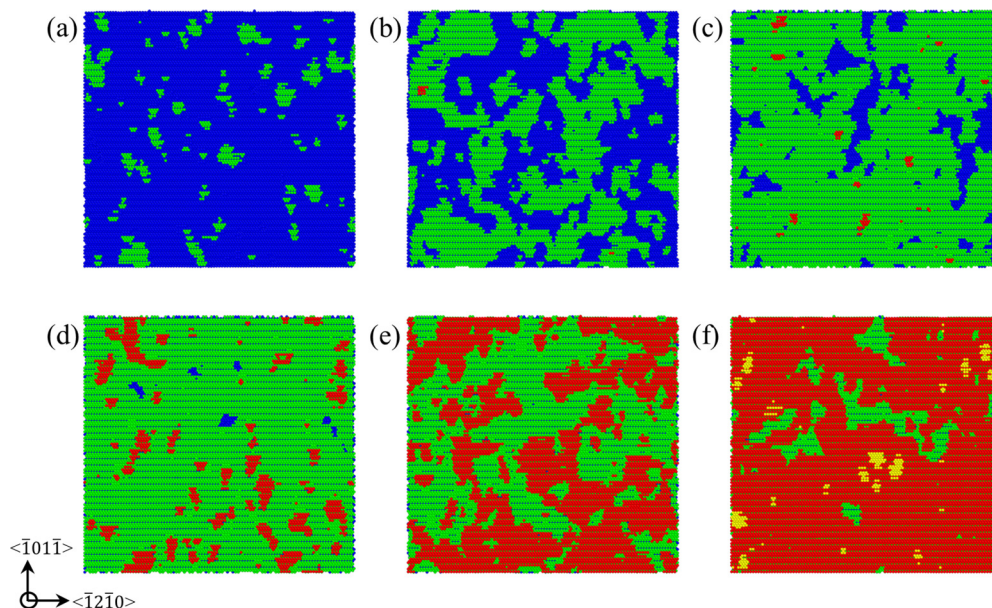


FIG. 5. Disconnection terrace nucleation, growth, and coalescence at 500 K with an applied shear stress of 100 MPa. Atoms are colored in bands by Z position with blue, green, red, and yellow colors representing different sets of $\{10\bar{1}2\}$ planes parallel to the twin boundary.

terraces within the twin boundary plane. This mechanism is referred to as autocatalytic nucleation and shows that in the stress-driven regime, correlated nucleation events can occur and should be considered in models for twin growth. The importance of stress concentrations on autocatalytic behavior will be discussed further in Sec. IV. After several propagation and nucleation events, terraces with relatively arbitrary shapes nucleate at higher rate. This coincides with a linear regime for plastic strain rate [e.g., Fig. 2(a)]. The arbitrary shape of the disconnection terraces in this regime implies that disconnection line tension plays a minor role.

At higher temperature but lower shear stresses, the frequency of disconnection terrace nucleation is significantly higher resulting in nucleation of many irregularly shaped terraces that simultaneously interact within the $\{10\bar{1}2\}$ twin boundary plane, as shown in Fig. 5 for the case $\tau_{YZ} = 100$ MPa and $T = 500$ K. The irregular shape of the terraces in Fig. 5 implies a relatively low excess energy of the disconnection core. At this temperature, new terrace formation is considered to be due to both autocatalytic terrace nucleation and spontaneous formation due to entropic effects. Interestingly, double layers are sometimes observed where a disconnection terrace nucleates on top of an existing disconnection terrace that is actively expanding, indicating that the twin boundary does not necessarily return to a pristine state at a different Z elevation before continued terrace nucleation.

C. Model for shear-driven motion of the twin boundary

A velocity law for the shear-driven motion of the $\{10\bar{1}2\}$ twin boundary is proposed that accounts for shear stress, temperature, and size dependence. Altogether, the effective twin boundary velocity results from both nucleation of new terraces and growth of existing terraces. Let n_t and A_t denote the instantaneous areal terrace density and their individual area, respectively. Further, if one denotes with h the height of

the elementary $b_{2/2}$ disconnection associated with the motion of the twin boundary, measured in the prior sections from atomistic simulations, then the twin boundary velocity can be written as

$$v = h(\dot{n}_t A_t + n_t \dot{A}_t). \quad (1)$$

The first term in Eq. (1) corresponds to that proposed by Luque *et al.* [15]. In their work, the authors assume (i) that each nucleated terrace is in equilibrium and has an assumed square or rectangular shape, (ii) that nucleation events are statistically uncorrelated, and (iii) that the attempt frequency associated with terrace nucleation decreases linearly with the number of atoms in the nucleated terrace. Altogether, this leads to an Arrhenius-type model for twin growth rate where the preexponential factor scales to the fourth power with the imposed shear stress.

Within the driving force regime studied in this work, which can include autocatalytic behavior as shown in Figs. 4 and 5, it is postulated that when a steady state is reached, the areal density of terraces remains constant, neglecting the first term of Eq. (1), such that the expansion of twin terraces becomes the rate limiting factor. Further, the equilibrium areal terrace density is given by the product of the number of sites per unit area n_A , the area simulated, and the probability of nucleation given by the Arrhenius law in which enthalpy is written as $\Delta H = \Delta U_0 - \tau v_A$. Here, v_A is the activation volume for the nucleation of disconnection loops and ΔU_0 denotes their formation energy. Note that n_A could depend on stress. While in the autocatalytic regime these considerations appear to be unnecessary, this may not be the case in the nucleation-starved regime (i.e., low stress and low temperatures). Furthermore, the expansion of each terrace can be simply written via a drag law linearly relating the velocity of disconnections, with Burgers vector b , to the imposed resolved shear stress via a temperature dependent mobility M . This mobility is to be interpreted as an effective mobility in the $\{10\bar{1}2\}$ twin plane

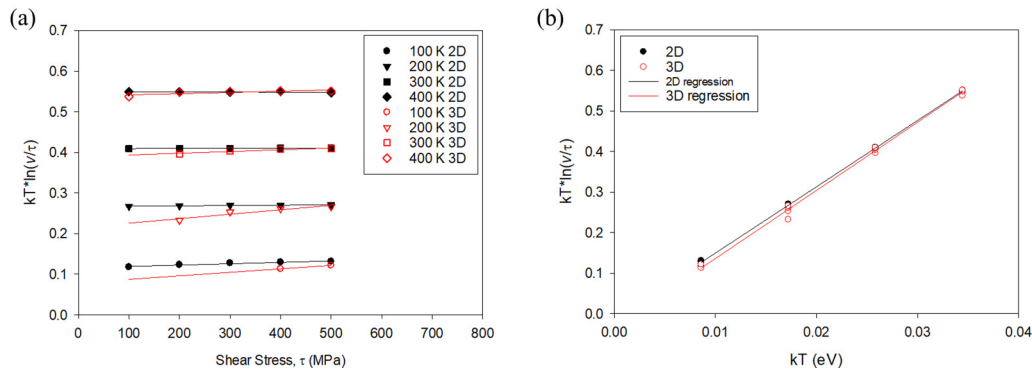


FIG. 6. Application of Eq. (2) to the MD simulation data in 2D and 3D. Manipulation of Eq. (2) provides (a) the activation volume for 2D and 3D simulation models (slope of each curve) and (b) the activation energy ΔU (Y -axis intercept) and the mobility M (slope of the curve).

for each disconnection terrace. In practice, the dependence of mobility on the disconnection character must be assessed. With these considerations, and if r_{eff} is defined as the mean effective radius of terraces,

$$v = 2\pi r_{\text{eff}} h n_a M b \tau \exp\left(\frac{-\Delta U_0 + \tau v_A}{kT}\right). \quad (2)$$

In Eq. (2), k is Boltzmann's constant, T denotes the temperature, and b refers to the norm of the Burgers vector of the elementary disconnection. By rearranging Eq. (2), both activation volume and activation energy can be estimated from MD simulation results. Figure 6(a) shows $kT \ln(v/\tau)$ versus the applied shear stress τ , for 2D and 3D simulation models. The slope provides the activation volume v_A , which is not expected to depend on temperature. From the 2D and 3D MD simulation results, this is true at the highest temperatures considered (300 and 400 K). For 2D simulations, the activation volume is found to be relatively constant, with a best fit yielding an activation volume of approximately $0.08b^3$ at $T = 100$ K and essentially zero at a temperature of 400 K. For 3D simulations, the activation volume varies from approximately $0.26b^3$ at the lowest temperatures considered down to $0.075b^3$ at 400 K. In summary, the dependence of the activation volume on temperature is particularly weak and occurs only in the nucleation-starved regime for which both terms of Eq. (1) should be considered to better capture the curvature in Figs. 2(b) and 3.

Figure 6(b) shows $kT \ln(v/\tau)$ versus the kinetic temperature, kT , for both 2D and 3D simulation models. The Y axis intercept of each regression line provides the activation energy ΔU_0 associated with the terrace nucleation process, under the assumption that the activation volume is very small, which is confirmed in Fig. 6(a). For 2D simulations, the activation energy is 0.014 eV, while for 3D simulations the activation energy is 0.032 eV. Thus, there is a measurable difference between both the activation energy (as well as the activation volume) between 2D and 3D simulation models, underscoring the importance of terrace geometry in the shear-driven motion of the $\{10\bar{1}2\}$ twin boundary. Ultimately, the atomistic simulation data for the twin boundary velocity, shown in Figs. 2(b) and 3, support the validity of Eq. (2). Using the activation volumes and energies computed from Fig. 6, the model accurately predicts shear stress and temperature dependence in the high-driving-force regime, but fails to capture the decay in

twin boundary velocity below the transition to a disconnection loop nucleation-starved regime [13–15] for twin boundary migration.

IV. DISCUSSION

In 2D, the formation energy of disconnection terraces on the $\{10\bar{1}2\}$ twin boundary can be written as [10]

$$U_0 = 2E_{\text{core}} + E_{\text{int}}. \quad (3)$$

Here E_{core} and E_{int} denote the core energy of each disconnection and the interaction energy between disconnections, respectively. Further, assuming isotropic elasticity, E_{int} can be estimated as [41]

$$E_{\text{int}} = \frac{kb^2}{4\pi} \ln\left(\frac{w}{r_c}\right), \quad (4)$$

where k denotes a constant with units of energy per volume, w is the distance between the disconnections, and r_c is the core radius. To assess the difference between the energy barrier extracted from MD simulations and energy barriers associated with the nucleation of individual terraces, the formation energy of individual disconnection terraces is computed in 2D, as shown in Fig. 7. The core contribution alone is computed

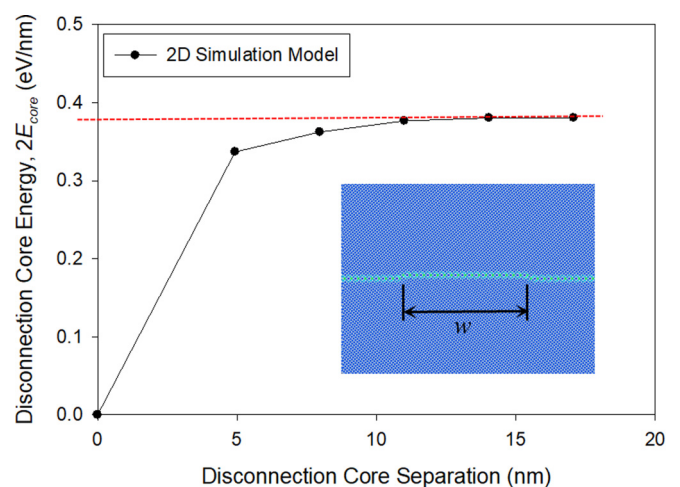


FIG. 7. Energy of the disconnection cores ($2E_{\text{core}}$) as a function of separation distance between disconnection cores using 2D models.

to be 0.38 eV/nm. By comparison, the current 2D simulations predict an effective activation energy of 0.044 eV/nm. This largely suggests that the nucleation of terraces is correlated in the stress and temperature regime studied, as opposed to a nucleation-starved regime [15] corresponding to the first term of Eq. (1). Similar conclusions can be made for the 3D case, as the formation energy of a disconnection loop of critical size is expected to be much larger than the activation energy extracted from MD simulations in Sec. III. In fact, Race *et al.* [13] showed that a nucleation-based model overpredicts the energy barrier for GB migration at high driving forces, likely because it does not consider correlated events. This significant difference can be rationalized as follows. First, the activation volume extracted from the MD simulations is particularly small, which explains why a stable terrace can be generated locally by stress concentrations. Second, once the first disconnection terrace is generated, this terrace will naturally provide the local stress concentration that contributes to the generation of new disconnection terraces, due to the stress field associated with the disconnection [42], thereby providing an additional driving force. This is the essence of the autocatalytic process, as previously identified for the case of twin nucleation from the grain boundary sources [21,22]. From a constitutive modeling viewpoint, capturing the effects of this autocatalytic process entails that field variables quantifying the Helmholtz free energy in the system be described with nanometer length scale resolution.

To appreciate the pertinence of the autocatalytic regime, consider the three-stage sequence leading to twin domain thickening, consisting of disconnection loop nucleation, transverse growth, and coalescence. In a continuous medium, the shear strain associated with the twin transformation will induce a back shear stress applied by the host parent or by the neighboring crystals. These reaction stresses have been shown to be greater than 100 MPa [18–20] and they will affect both the lateral propagation of the twin and its thickening process. Indeed, during the forward propagation of the twin domain, the stress states at the tip of a twin and away from the tip will differ significantly. One can estimate the stress field surrounding a twin domain embedded in a matrix phase by using an Eshelby inclusion approach. Assuming elasticity and an ellipsoidal twin shape, the resolved shear stress on the twinning plane ahead of the twin tip will be positive, and well in excess of 100 MPa, while it should be negative midway across the twin. With this, it is expected that the propagation of the twin tip will be accompanied by the nucleation and motion of disconnection terraces on coherent twin planes. Given the high stress state at the twin tip, this sequence of events will occur in the autocatalytic nucleation regime. It suggests that twins thicken during the lateral propagation of their tip, consistent with other atomistic scale simulations [43].

Finally, during the thickening stage and considering the case when the twin is connected to grain boundaries, given

the small effective activation volumes and activation energies extracted from MD simulations, the autocatalytic regime could be triggered by both intergranular stresses (type II) and transgranular stresses (type III) associated with the dislocation microstructure. This in turn rationalizes the particularly complex shapes adopted by tensile twins in Mg and Mg alloys.

V. CONCLUSIONS

Using molecular dynamics simulations, the mechanisms associated with shear-driven motion of the $\{10\bar{1}2\}$ mirror twin boundary in Mg are characterized, and the importance of 3D model geometry on shear-driven motion is emphasized. The twin boundary migrates in the direction normal to the coherent twin plane via the nucleation, growth, and coalescence of disconnection terraces. This study reveals the presence of an autocatalytic regime for twin growth, whereby new terrace nucleation can be triggered by the growth of existing terraces on the twin boundary plane, which leads to small (<0.1 eV) effective activation barriers for nucleation of terraces. This suggests that twin growth is dependent on local stress concentrations, which may arise as intragranular stresses from the presence of dislocations, or grain neighbor induced intergranular stresses. With this, it is to be expected that local twin growth bursts could occur in the local vicinity of stress concentrations, if these are aligned with the twinning shear direction and twin plane. Thus, one would expect fully 3D twin domains to have particularly irregular shapes, consistent with 3D electron backscatter diffraction (EBSD) observations [44].

Further, a model is proposed to describe $\{10\bar{1}2\}$ effective twin boundary velocity during shear-driven motion. Molecular dynamics simulations are used to compute activation energies and activation volumes for both 2D and 3D simulation geometries, confirming that the kinetics of twin propagation must consider the 3D nature of disconnection nucleation, growth, and coalescence. Finally, it is noted that results of this study apply to twin thickening by shear-stress-driven migration of the coherent plane. This mechanism does not exclude other possible terrace-nucleation mechanisms, such as dislocation-twin reactions. Furthermore, the disconnection terrace nucleation and expansion may also assist forward and lateral twin propagation [3], which should also be treated within a 3D framework. These calculations, however, do not provide information about the latter mechanisms.

ACKNOWLEDGMENTS

L.C. and C.N.T. acknowledge support of the U.S. Department of Energy, Office of Basic Energy Sciences Project No. FWP 06SCPE401. D.E.S. acknowledges the University of Florida Research Computing for providing computational resources used for obtaining the research results reported in this publication.

[1] J. W. Christian and S. Mahajan, *Prog. Mater. Sci.* **39**, 1 (1995).

[2] M. Gong, G. Liu, J. Wang, L. Capolungo, and C. N. Tomé, *Acta Mater.* **155**, 187 (2018).

[3] Y. Liu, N. Li, S. Shao, M. Gong, J. Wang, R. J. McCabe, Y. Jiang, and C. N. Tomé, *Nat. Commun.* **7**, 11577 (2016).

[4] L. Leclercq, L. Capolungo, and D. Rodney, *Mater. Res. Lett.* **2**, 152 (2014).

- [5] A. Ostapovets and A. Serra, *Philos. Mag.* **94**, 2827 (2014).
- [6] J. P. Hirth, R. C. Pond, and J. Lothe, *Acta Mater.* **54**, 4237 (2006).
- [7] J. P. Hirth, J. Wang, and C. N. Tomé, *Prog. Mater. Sci.* **83**, 417 (2016).
- [8] A. Rajabzadeh, F. Momprou, M. Legros, and N. Combe, *Phys. Rev. Lett.* **110**, 265507 (2013).
- [9] H. A. Khater, A. Serra, R. C. Pond, and J. P. Hirth, *Acta Mater.* **60**, 2007 (2012).
- [10] E. Martinez, L. Capolungo, and C. N. Tomé, *Phys. Rev. Mater.* **2**, 083603 (2018).
- [11] J. W. Cahn, Y. Mishin, and A. Suzuki, *Acta Mater.* **54**, 4953 (2006).
- [12] N. Combe, F. Momprou, and M. Legros, *Phys. Rev. B* **93**, 024109 (2016).
- [13] C. P. Race, J. von Pezold, and J. Neugebauer, *Phys. Rev. B* **89**, 214110 (2014).
- [14] R. Hadian, B. Grabowski, C. P. Race, and J. Neugebauer, *Phys. Rev. B* **94**, 165413 (2016).
- [15] A. Luque, M. Ghazisaeidi, and W. A. A. Curtin, *Acta Mater.* **81**, 442 (2014).
- [16] A. Serra and D. J. Bacon, *Philos. Mag. A* **73**, 333 (1996).
- [17] A. Serra, D. J. Bacon, and R. C. Pond, *Acta Mater.* **47**, 1425 (1999).
- [18] M. Arul Kumar, M. Gong, I. J. Beyerlein, J. Wang, and C. N. Tomé, *Acta Mater.* **168**, 353 (2019).
- [19] M. Arul Kumar, A. K. Kanjarla, S. R. Niezgoda, R. A. Lebensohn, and C. N. Tomé, *Acta Mater.* **84**, 349 (2015).
- [20] M. Arul Kumar, I. J. Beyerlein, and C. N. Tomé, *Acta Mater.* **116**, 143 (2016).
- [21] H. Liu, F. X. Lin, P. Zhao, N. Moelans, Y. Wang, and J. F. Nie, *Acta Mater.* **153**, 86 (2018).
- [22] M. Arul Kumar, I. J. Beyerlein, R. J. McCabe, and C. N. Tomé, *Nat. Commun.* **7**, 13826 (2016).
- [23] S. Plimpton, *J. Comput. Phys.* **117**, 1 (1995).
- [24] A. Stukowski, *Model. Simul. Mater. Sci. Eng.* **18**, 015012 (2010).
- [25] Z. Wu, M. F. F. Francis, and W. A. A. Curtin, *Model. Simul. Mater. Sci. Eng.* **23**, 015004 (2015).
- [26] Y. Kim, N. J. Kim, and B. Lee, *CALPHAD Comput. Coupling Phase Diagrams Thermochem.* **33**, 650 (2009).
- [27] D. Y. Sun, M. I. Mendeleev, C. A. Becker, K. Kudin, T. Haxhimali, M. Asta, J. J. Hoyt, A. Karma, and D. J. Srolovitz, *Phys. Rev. B* **73**, 024116 (2006).
- [28] X. W. Zhou, R. A. Johnson, and H. N. G. Wadley, *Phys. Rev. B* **69**, 144113 (2004).
- [29] D. E. Spearot and D. L. McDowell, *J. Eng. Mater. Technol.* **131**, 041204 (2009).
- [30] M. A. Tschopp and D. L. McDowell, *Philos. Mag.* **87**, 3871 (2007).
- [31] J. D. Rittner and D. N. Seidman, *Phys. Rev. B* **54**, 6999 (1996).
- [32] Z. Pei, X. Zhang, T. Hickel, M. Friák, S. Sandlöbes, B. Dutta, and J. Neugebauer, *npj Comput. Mater.* **6**, 1 (2017).
- [33] S. Hagege, M. Mori, and Y. Ishida, *J. Phys. Colloq.* **51**, 161 (1990).
- [34] J. R. Morris, Y. Ye, and M. H. Yoo, *Philos. Mag.* **85**, 233 (2005).
- [35] Y. Wang, L.-Q. Chen, Z.-K. Liu, and S. N. Mathaudhu, *Scr. Mater.* **62**, 646 (2010).
- [36] Z. Pei, H. Sheng, X. Zhang, R. Li, and B. Svendsen, *Mater. Des.* **153**, 232 (2018).
- [37] S. Melchionna, G. Ciccotti, and B. L. Holian, *Mol. Phys.* **78**, 533 (1993).
- [38] R. J. Kurtz, R. G. Hoagland, and J. P. Hirth, *Philos. Mag. A* **79**, 683 (1999).
- [39] D. L. Olmsted, L. G. Hector, Jr., W. A. Curtin, and R. J. Clifton, *Model. Simul. Mater. Sci. Eng.* **13**, 371 (2005).
- [40] J. Cho, J. Molinari, and G. Ancaux, *Int. J. Plast.* **90**, 66 (2017).
- [41] O. MacKain, M. Cottura, D. Rodney, and E. Clouet, *Phys. Rev. B* **95**, 134102 (2017).
- [42] J. Han, S. L. Thomas, and D. J. Srolovitz, *Prog. Mater. Sci.* **98**, 386 (2018).
- [43] B. Xu, L. Capolungo, and D. Rodney, *Scr. Mater.* **68**, 901 (2013).
- [44] A. Fernández, A. Jérusalem, I. Gutiérrez-Urrutia, and M. T. Pérez-Prado, *Acta Mater.* **61**, 7679 (2013).